crystals

MDPI

Article

A Bi-Pronged Attempt at Normalizing DL-EPRT Vis-à-Vis Grain-Boundary/σ-Phase Locales in Thermally Sensitized UNS S32205 Duplex Stainless Steel

Abdulla F. Alshater [1,*], Abbas S. Hakeem [2], Ablikim Bake [3], Hatim D. Mohamed [4], Hosni M. Ezuber [1], Alia Mustafa [5], Ruqayah R. Alnasser [1], Mezna K. Al Ruwaihi [1], Aysha I. Rashdan [1], Fatema A. Jaberi [1] and Khadija S. Bahar [1]

[1] College of Engineering, University of Bahrain, Isa Town P.O. Box 32038, Bahrain; halzubair@uob.edu.bh (H.M.E.); alnasser-606@hotmail.com (R.R.A.); malrowaihi@sce.gov.bh (M.K.A.R.); aysha_rashdan@outlook.com (A.I.R.); 951210505@moe.bh (F.A.J.); khadoojbahar@gmail.com (K.S.B.)
[2] Interdisciplinary Research Center for Hydrogen Technologies & Carbon Management (IRC-HETCM), King Fahd University of Petroleum and Minerals, Dhahran 31261, Saudi Arabia; ashakeem@kfupm.edu.sa
[3] Institute for Biomedicine and Glycomics, Griffith University, Southport, QLD 4215, Australia; a.bake@griffith.edu.au
[4] Core Research Facilities (CRF), King Fahd University of Petroleum and Minerals, Dhahran 31261, Saudi Arabia; dmhatim@kfupm.edu.sa
[5] College of Science, University of Bahrain, Sakhir P.O. Box 32038, Bahrain; amkhan@uob.edu.bh
* Correspondence: aalshater@uob.edu.bh

Abstract: In a quest to vet UNS S32205 as a potential structural material to serve moderate-to-high temperature operations of NPP auxiliary components, the DL-EPR test was exploited. A bifronted scheme comprised of 650 and 850 °C discrete treatments intended to explore progressive eutectoid decomposition and degree-of-sensitization (DoS) scenarios was adopted. The nuance witnessed with yet another dual approach—the Cihal- and image processing (IP)-normalized signal landscape—was rationalized through its attribution to culprit microstructures. This was sought, inter alia, in the vicinity of grain boundaries and σ-phase inclusions by virtue of postmortem FESEM, STEM-EDX, HRTEM SAED and XRD ascertainment. Discernable reactivation-kinetics resurgence was believed to mark the onset of deleterious σ-phase dissolution. This only came into fruition with longer ageing times (8–17 h) at 650 °C and succumbed to prematurely (1 h), and at DC biases more cathodic than −0.25 VAg/AgCl with the 850 °C counterpart. Opportune corroboration was offered in i_r/i_a breakaway for the respective conditions, which was unveiled to be particularly pre-emptive (5 h) with IP- vs. Cihal-normalized peers (8 h) related to the 650 °C condition. Meanwhile, the 850 °C condition endured a similar surge after as little as 1 h of ageing across the board, which hints at concomitant sigma-phase culpability.

Keywords: degree of sensitization; double-loop electrochemical potentiokinetic reactivation; normalization; Cihal method; image processing

Citation: Alshater, A.F.; Hakeem, A.S.; Bake, A.; Mohamed, H.D.; Ezuber, H.M.; Mustafa, A.; Alnasser, R.R.; Al Ruwaihi, M.K.; Rashdan, A.I.; Jaberi, F.A.; et al. A Bi-Pronged Attempt at Normalizing DL-EPRT Vis-à-Vis Grain-Boundary/σ-Phase Locales in Thermally Sensitized UNS S32205 Duplex Stainless Steel. *Crystals* **2024**, *14*, 692. https://doi.org/10.3390/cryst14080692

Academic Editor: Mingyi Zheng

Received: 27 June 2024
Revised: 20 July 2024
Accepted: 24 July 2024
Published: 29 July 2024

1. Introduction

The realm of degree-of-sensitization (DoS) electrochemical assessment has witnessed a plethora of emerging techniques, yet each riddled with an overambitious set of claims towards conferring an accurate quantitative address upon the issue. Though crucial precursors to current, more-meticulous techniques in the chronological hierarchy, potentiodynamic anodic polarization [1], potentiostatic etching [2–5], and abstract single- and double-loop EPR [6–8] have failed to deliver on electrochemical signal-normalization efforts. This is because such traditional undertakings were seldom guided by deliberate schemes that account for the inevitable inconsistencies inherent to grain-boundary physical dimensions across materials. This not to mention the ineptitude of sensitively gauging the

DoS once frontiers of severe detriment are infringed upon [9], or at least remain faithful to the non-destructive merits underpinning the sought-after endeavors [2]. For example, while the honor of historical precedence in quantitatively addressing the DoS from an electrochemical perspective might be bestowed upon potentiodynamic anodic polarization, the latter remains an underdeveloped technique at present. This is because it stands somewhat afflicted by reports of controversial gauging potency pertaining to the very phenomenon it was inherently set to critique [10]. Moreover, conflicting testaments might be stumbled upon in the literature attesting to an intimate association between the rise in the DoS and dwindling critical and passivation current densities at times [11] while in other instances refuting any discernable interdependency to that effect [12]. Meanwhile, efforts that had formerly sought refuge in setting the mere emergence of a prominent second peak as a criterion had been proven to be notoriously ill-equipped to convincingly gauge the milder extremity of sensitization spectrum [13]. Alternatively, the potentiostatic-etching technique risks casting an overly trivialized methodology upon forecasting extents of chromium depletion across broadly disseminated grain-boundary locales (with characteristic Cr-denuding contrast) through mere correlation with passivation potential [2–5]. Thus, the aforementioned preliminary approaches might easily fall victim to looming irreproducibility that immediately arises in conjunction with the meagre departure from handling a single batch of materials, let alone contrasting alloy compositions. This is by virtue of the reliance on absolute cumulative-charge monitoring to subsequently correlate with the DoS [13,14], as opposed to the relativistic attribution of charge measured to vulnerable microstructural locales, as embraced by EPR-based techniques. Admittedly, signs of well-placed discretion whilst quoting reactivation charge-density peaks conjunct with grain-boundary area began to gain recognition in the wake of being advocated by Clarke et al. [15,16], amid the establishment of the single-loop variant in EPR testing. A breakthrough that later morphed into a double-loop version of the approach in concern was documented by Akashi et al. [17,18]. However, the SL-EPR technique remains troubled by an undesirable association with the extent of maturity pertaining to the metallographic surface finish. Furthermore, early attempts aimed at the normalization of electrochemical measurements had inadvertently subscribed to a grave unwarranted assumption. The postulate in concern argued for the adequacy of considering electrical charge to emanate from sensitized grain boundaries that are consistent in the breadth of their Cr-depletion profiles whilst percolating unscathed along the entirety of such boundary networks—that is, during the latter's span across extremities of a given specimen. This is not to mention depicting grain geometries as perfect spheres throughout. A precedent that incentivized the reliance on the standardized Cihal scheme for grain-size determination documented in ASTM E112-13 [19] and BS EN ISO 643:2012 [20] in normalization endeavors pertaining to the dual-faceted EPR technique [6,21]. The case need not be made for the thwarting effect brought about by such a vast oversimplification in depriving the technique at hand from attending to stepped (unsensitized) stainless-steel microstructures. This is in addition to dual-stepped and non-continuously ditched (intermediately sensitized) stainless steels, unveiling the extent of sensitization as per ASTM A262 practice A [2]. The vacuum brought about by the inept normalization approach described thus far calls upon a subjective boundary-by-boundary dimensional critique of intergranular vicinity detriment. Image processing might offer potent provision as it relates to such settings. This is as indiscriminatory perception of the odds for sensitization pertaining to populations of grain boundaries innately varying in extents of lattice-site coincidence and compactness had been proven unwise in peer investigatory endeavors [22–30]. Hence, to steer clear of enduring such a pitfall, it was incumbent upon particular studies to opt for a bypass of the problematic fixtures on grain-boundary width, whether at $2 \times (5 \times 10^{-5})$ cm for SL-EPR [15,16] or 10^{-4} cm for DL-EPR [9,17] contemporaneously. It is owing to such an adjustment that normalizations predicated upon the grain-boundary area (GBA) were suspended in favor of their network length (GBL)-based peers [31]. That is with the all-encompassing drive behind such a measure being the abundantly verified discrepancies between widths of Cr-depletion profiles

traversing grain boundaries and the often-broader spread for observed ditching at those very locales. Amongst the structural materials subjected, albeit somewhat sparingly, in the literature to the broad spectrum of DoS assessment endeavors, is duplex stainless steel. The most rudimentary of these is the UNS S32205 heat of DSS [32–36], which enjoys the perks of a bi-fronted ferrite/austenite makeup, rendering the alloy in display with enhanced resistance against localized corrosion whilst remaining mechanically robust. The latter, however, runs the risk of weathering operating conditions of detriment that potentially pave the way for long-term thermal ageing—that is, if we are to indulge in contemporary enthusiasm towards deploying DSS in serving auxiliary, yet critical, components of the nuclear industry [37]. This entails the incorporation of UNS S32205 in fabricating the likes of primary loop coolant pipes [38], reactor vessel internals [39,40], and interim wet storage pond walls [41] that stand complementary to NPP processes. As far as microstructural features of particular interest in UNS S32205 are concerned, intergranular chromium carbide and intragranular sigma-phase precipitate vicinities are infamous for Cr-depletion and often act as precursors to corrosion detriment [38,42]. With the scene set as such, it is unambiguous that the temperature-induced inclinations by ferrite islands within the duplex matrix towards undergoing variable extents of eutectoid decomposition would assume prime attention [32,33]. That is, in as far as contrasting proportions of regenerated austenite—highly accommodating of carbon atoms as interstices—to sigma phase that might come into fruition. It is in the spirit of establishing the means to facilitate normalized depictions of the DoS through which the inherent variability in sizes/span of electrochemical dissolution locales are subjectively accounted for that this work was embarked upon. To that end, the incautiously simplistic customary practice of DoS normalization was rendered a utility that lends itself to the opportune corroboration of a superiorly IGA-subjective take on the very normalization endeavor sought.

2. Materials and Methods

Grade UNS S32205 duplex stainless steel of composition, as outlined in Table 1, was made to endure a homogenizing preliminary solution annealing treatment at 1050 °C for 30 min.

Table 1. Chemical composition (wt%) of UNS S32205 grade of duplex stainless steel.

C	Si	Mn	P	S	Cr	Ni	Mo	N	Cu	Ti	Ce	Fe
0.016	0.39	1.43	0.022	0.001	22.39	5.7	3.19	0.178	0.2	0.001	0.002	66.48

The material was then subjected to two distinct sensitization temperatures, namely 650 and 850 °C, aimed at exploring the microstructural features emanating from benign and mature degrees of thermal sensitization, respectively, in conjunction with the extent of ferrite decomposition. To that end, a wide spectrum of ageing times was deployed, spanning 1, 3, 5, 8 and 17 h. The preliminary solution annealing precursing the two subsequent sensitization treatments, namely at 650 and 850 °C, will be referred to as 'heat treatments 1 and 2′, respectively, throughout this manuscript. The material as supplied was 1.5 cm diameter rigid rods that extended 1 m in length. In attending to electrochemical testing needs, the as-received geometry was eventually reduced down to cubes that were 5 mm per side. Fabrication processes were optimized to minimize adverse thermo-mechanical effects by restricting the cutting-tool feed rate and maintaining ample cooling throughout the operation of a Buehler Isomet low-speed saw. In rendering samples electrically conductive, paving the way for subsequent electrochemical testing, Nichrome wires were spot-welded onto samples, where the joint was then electrically insulated via plastic sheathing. Electrochemical samples proceeded to be cold-mounted into epoxy resin to ultimately expose a typical 0.277 ± 0.044 cm^2 of the alloy. All samples were then taken down to a 4000-grit finish before being ultimately polished using 0.25-micron diamond paste.

A typical three-electrode electrochemical setup was adopted with DSS, Ag/AgCl half-cell and a platinum wire/foil assuming the role of the working, reference and counter electrodes, respectively. Conventional double-loop electrochemical potentiokinetic reactivation testing (DL-EPRT) was deployed to offer a quantitative, albeit inaccurate, preliminary rendition of the degree of sensitization (DoS). The test was administered in an electrolyte comprising 0.5 M H_2SO_4 and 0.01 M KSCN at ambient temperature. A potentiodynamic sweep was commenced from realms slightly cathodic to an OCP that lies in the vicinity of −0.34 VAg/AgCl. The potential was then made to encroach upon increasingly anodic territories until it soared as high as 0.25 VAg/AgCl, before traversing back to where the scan was originally initiated. A scan rate of 1.67 mV/s was maintained throughout.

A critique of morphologies and deteriorative microstructural features on samples postmortem related to DL-EPR testing was sought in an effort to verify the sources of the electrochemical signals amassed. This was realized with the aid of a TESCAN Lyra 3 (TESCAN, Brno, Czech Republic) field emission (FE-) and a ZEISS EVO LS10 (LaB6-, ZEISS, Oberkochen, Germany) scanning electron microscope (SEM). Chemical composition scrutiny was administered through area and line scans across features of interest using a Thermo Fisher Scientific Quattro FESEM (in STEM mode, Thermo Fisher Scientific, Waltham, MA, USA) equipped with means for energy dispersive X-ray Spectroscopy (EDS) utilizing an Oxford Instruments (X-MaxN, Abingdon, UK) silicon drift detector. Both topographical and microchemical critique were conducted using an accelerating voltage of 20 kV [43,44]. Meanwhile, thin TEM lamellae were extracted from samples pertaining to key conditions of interest with the aid of FEI HELIOS G3 Dual-Beam FIB-SEM (FEI Company, Hillsboro, OR, USA).

Unveiling a reciprocal lattice for localized microstructures of interest was facilitated by way of selected area electron diffraction (SAED) with the aid of a JEOL JEM-2100F 200 kV (JEOL Ltd., Tokyo, Japan) transmission electron microscope (TEM). The indexing of diffraction patterns and generation of 3D renditions of complex structures were rendered into existence with the aid of an automated crystallographic deciphering toolbox (CrysTbox) courtesy of Klinger et al. [45–48]. The preliminary ascertainment of crystallographic features distinctive of the phases anticipated was facilitated by way of X-ray diffractometry (XRD) utilizing a Rigaku MiniFlex X-ray diffractometer (Tokyo, Japan). The latter was deployed in conjunction with Cu Kα1 radiation (γ = 0.15416 nm), a tube current of 10 mA and an accelerating voltage of 30 kV [49–51].

It is by virtue of the abstract approach to DL-EPR testing being solely predicated upon the total exposed working electrode area, and as such, effectively dismissive of inevitable discrepancies in grain-boundary dimensions, that endeavors aimed at normalization of i_r/i_a responses were sought in this work. A bifrontal attempt was made to account for grain-boundary area (*GBA*) and length (*GBL*) in discrete incidences whilst addressing i_r/i_a firstly through ISO 12732 (based on the Cihal method) [21]. The latter is centered around standard grain-size measurement techniques, the outcome of which contributes towards the rendering into fruition a DoS that is subjective of a given unique, yet averaged, extent of attack at vulnerable microstructural features. ISO 12732 formulates the normalization approach as follows:

Cihal method-based DoS normalization (predicated upon *GBA*):

$$\left(\frac{I_r}{I_a}\right)_{GBA} = \frac{\frac{I_r}{S_{GBA}}}{\frac{I_a}{A_S}} = \frac{\frac{I_r}{S_A * A_S}}{\frac{I_a}{A_S}} = \frac{I_r}{S_A * I_a} = \frac{I_r}{I_a * 10^{-3} * \sqrt{2^{G+5}}} \quad (1)$$

Cihal method-based DoS normalization (predicated upon *GBL*):

$$\left(\frac{I_r}{I_a}\right)_{GBL} = \frac{\frac{I_r}{L_{GBL}}}{\frac{I_a}{A_S}} = \frac{\frac{I_r}{10 * L_A * A_S}}{\frac{I_a}{A_S}} = \frac{I_r}{10 * L_A * I_a} = \frac{I_r}{I_a * 10 * \sqrt{2^{G+5}}}\ (\text{cm}) \quad (2)$$

where 'I_r' is the peak current for the reactivation/reverse scan and 'I_a' is the peak current of the activation/forward scan, and both 'I_r' and 'I_a' are expressed in units of ($\mu A/cm^2$). 'S_A' is the grain-boundary area per unit of specimen area determined using the following formula:

$$S_A = 4 \times 10^{-3} * \sqrt{2^{G+1}} \quad (3)$$

'A_s' is the specimen area and 'SGBA' is the grain-boundary area, where both 'A_s' and 'S_{GBA}' are given in units of cm^2. 'S_{GBA}' might be computed as follows:

$$S_{GBA} = S_A * A_S \quad (4)$$

'L_A' is the length of grain-boundary network per unit of specimen area addressed in mm^{-1} and determined in accordance with the following formula:

$$L_A = \sqrt{2^{G+5}} \quad (5)$$

'L_{GBL}' is the grain-boundary network length in cm, which might be mathematically represented as follows:

$$L_{GBL} = 10 * L_A * A_S \quad (6)$$

'G' is the grain-size number in accordance with ISO 643 [20] that is determined using the Jeffries Planimetric method [19,52,53] with the aid of (ImageJ v1.52p) image processing software. This was realized by identifying a minimum of three circles, typically 60 microns in diameter, arbitrarily situated across widely dispersed positions on 'A_s' such that they hold within their confinement grain populations deemed characteristic of the structure and treatment at hand. At least two samples extracted from discrete batches of the material per condition were examined as described, and a threshold for statistical credibility was set as a minimum of 50 grains within circle constrictions for a given measurement. Jeffries factor 'f' was calculated as follows:

$$f = \frac{m^2}{A_C} \quad (7)$$

where 'm' is the magnification and 'A_C' is the area of a drawn circle for grain-size determination.

Secondly, an effectively more accurate rendition of the DoS reputably prone to unveiling archetypical electrochemical responses that reckon with innate discrepancies in extents of grain-boundary attack is that predicated upon normalization by way of AI (or computational) image processing. An identical statistical approach to that which advised the handling of measurements in the case of ISO 12732 normalizations was maintained in subjecting the very same range of samples to AI-based normalizations this time around. These were carried over to a Matlab 2019b routine, which, in turn, utilizes the image segmentation gray-thresholding trait of the software to recognize, sequester, and compute effective areas of grain-boundary attack from the remainder of bulk material.

3. Results and Discussion

This investigative endeavor commences by probing for DoS manifestations in wake of the scheme adopted for thermal ageing durations across the two sensitization temperatures adopted in this study. The indirect substantiation of corrosion detriment, namely that attained through tracking current density, is then corroborated by way of postmortem scanning electron microscopy—that is, with an eye on plausible coincidence with grain-boundary locales and the contemporaneous intragranular second-phase inclusion attack.

3.1. Crude Handling of DL-EPR Test Output

Inasmuch as laying the grounds for an incipient full-fledged argument in favor of a normalized approach is in order, a DoS critique will initially be perceived whilst deprived of any exogenous intervention (i.e., on a meagre i_r/i_a basis). This is an unrefined effort, the incentive behind which is for the latter to be refuted through evolution into the more

precise approach of Cihal method-based normalization. This would ultimately be allowed to morph into normalizations that are predicated upon stringent accounts of discrepancy in IGA dimensions in the quest to depict the DoS whilst enhanced by the fine touch of artificial intelligence that is image processing.

3.1.1. Heat Treatment 1

Figure 1 presents an outline of DL-EPR test findings representative of unstrained samples in the wake of incurring heat treatment 1. A persistent reverse peak 'i_r' is documented in coincidence with a DC bias that reproducibly resides in the vicinity of −0.15 V Ag/AgCl for profiles pertaining to all ageing times, Figure 1a–f. An auxiliary peak in current density is also embarked upon in profiles relating to 3 h ageing time, which proceeds to gradually encroach upon growingly cathodic realms before settling in the vicinity of −0.25 VAg/AgCl, Figure 1c–f. The profile for 3 h ageing treatment seems to simultaneously set a precedent that carries through to longer ageing times, hinting at an onset of modified cathodic reaction kinetics. This might be exemplified in the cathodic loop witnessed whilst traversing the reverse scan (c–f).

3.1.2. Heat Treatment 2

A thorough examination of the collective set of data emanating from sensitization at 850 °C showcased in Figure 2 yields more of a pronounced reverse peak resurgence at exceedingly cathodic realms in the vicinity of −0.25 V Ag/AgCl relative to the 650 °C treatment. Such a resurgence seems to be persistently in attendance alongside the conventional pinnacle at an overpotential of −0.15 V Ag/AgCl, which happens to be also offset towards more cathodic territories as opposed to their 650 °C counterparts. The phenomenon in concern, although considered a carryover from treatments at 650 °C, does nonetheless emerge in coincidence with ageing times as early as 1 hr. Yet a peculiar widening of reverse peaks for the reference condition well into the cathodic realms in concern (−0.25 V Ag/AgCl, that is) might hint upon precursors to the auxiliary event alluded to here. The described twin-spike incident, however, does grow in intensity with increased ageing time, only to be adjoined by an exacerbated cathodic loop relative to that reported for the 650 °C treatment, albeit at a delayed stage. This is because when it comes to the newfound complementary effect, it is the 5 h condition this time around that marks the onset of alterations to cathodic reaction kinetics. Contrast is being made here with the milder occurrence of the sort commencing somewhat prematurely in the vicinity of 3 h characteristic of the 650 °C treatment. Nonetheless, the two corrosion potentials 'E_{corr}' remain consistently encountered in the vicinity of 0.0 and −0.05 V Ag/AgCl as far as the 850 °C samples are concerned. A key discrepancy from observations made concerning the 650 °C samples is the premature bordering of the reactivation peaks onto their active/forward counterparts by 1 h this time around.

3.2. Postmortem Microstructural Critique

This endeavor aims to link electrochemical measurements with the identity and locale of effective microstructural detriment on specimens in the wake of weathering the spectrum of treatments adopted in this study. Vulnerable microstructures documented at this stage would serve to pave the way for subsequent normalization undertakings.

3.2.1. Heat Treatment 1

The reference and 1 h aged conditions appear to barely show any indications of sensitization and rather seem to surrender to stepped granular faceting indicative of a non-sensitized microstructure [2]. At such a stage, it would be somewhat premature to allude to legitimate second-phase formations, which might be evident should micrographs representative of the condition at hand be critiqued—see Figure 3a,b. This observation is also backed by an absence of the resurgence of reverse-current density peaking at cathodic DC bias realms of −0.25 V Ag/AgCl—see Figure 1a,b. The latter remains true

as ageing times progress up to 3 h, which is coincidentally also where discrete incidents of grain-boundary ditching are initially documented, as depicted in Figure 4a,b. Despite encroaching upon cathodic territories that border on −0.20 V Ag/AgCl, it is discernable that reactivation kinetics appear to shy away from presenting a pronounced/distinct second peak in coincidence with such cathodic overpotential—see Figure 1c. The inconsistent and arbitrarily disseminated intergranular attack observed with 3 h treatments does, in time, give in to unambiguous widening and grain circumference encompassment with progression towards 5 h, showcased in Figure 4c,d.

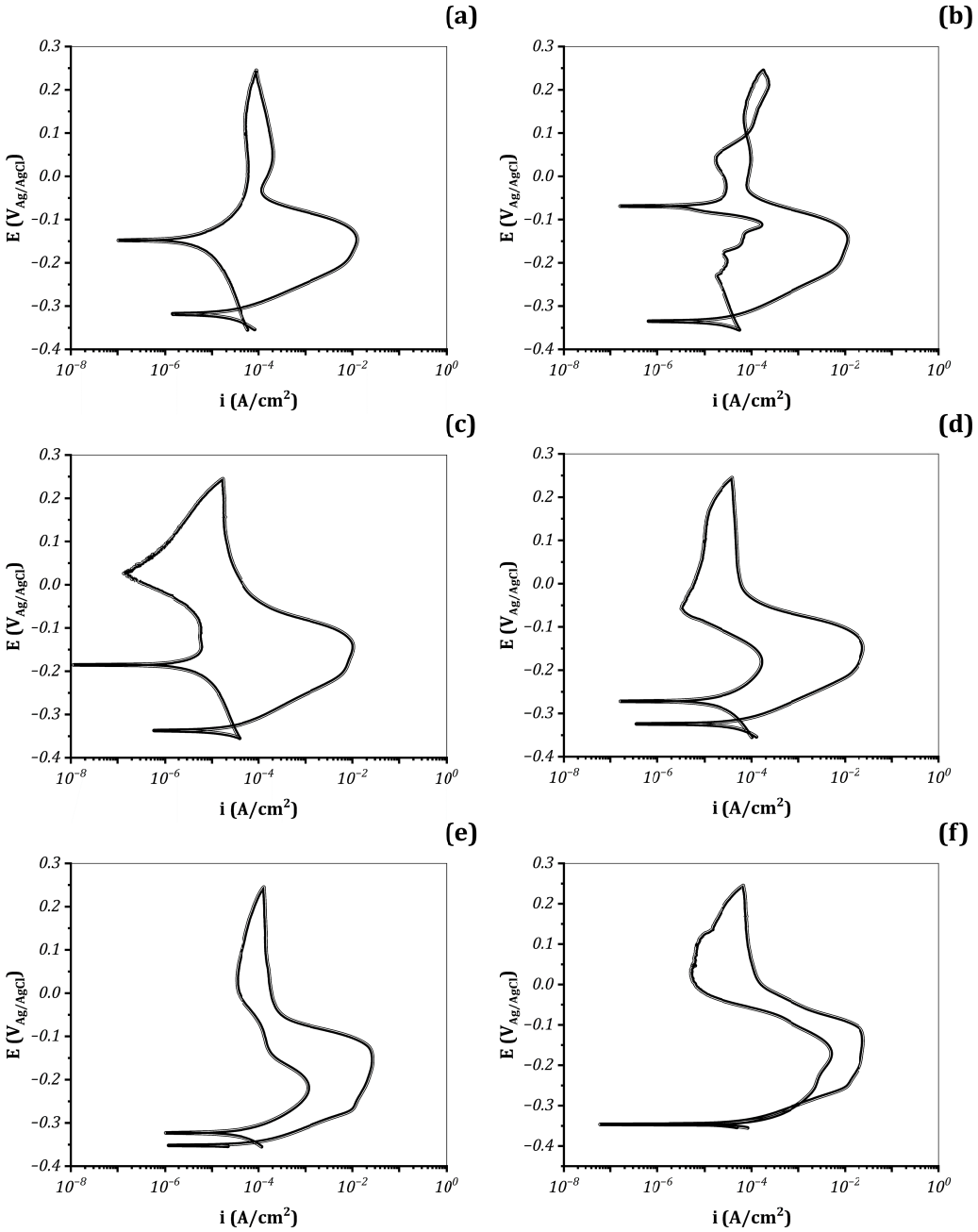

Figure 1. An outline of typical DL-EPR test profiles emanating from the unstrained DSS material in the wake of incurring the spectrum of sensitization treatments adopted in this investigative endeavor. These are namely, solution annealing at 1050 °C for half an hour followed by ageing at 650 °C for 0.0 h (**a**), 1 h (**b**), 3 h (**c**), 5 h (**d**), 8 h (**e**) and 17 h (**f**).

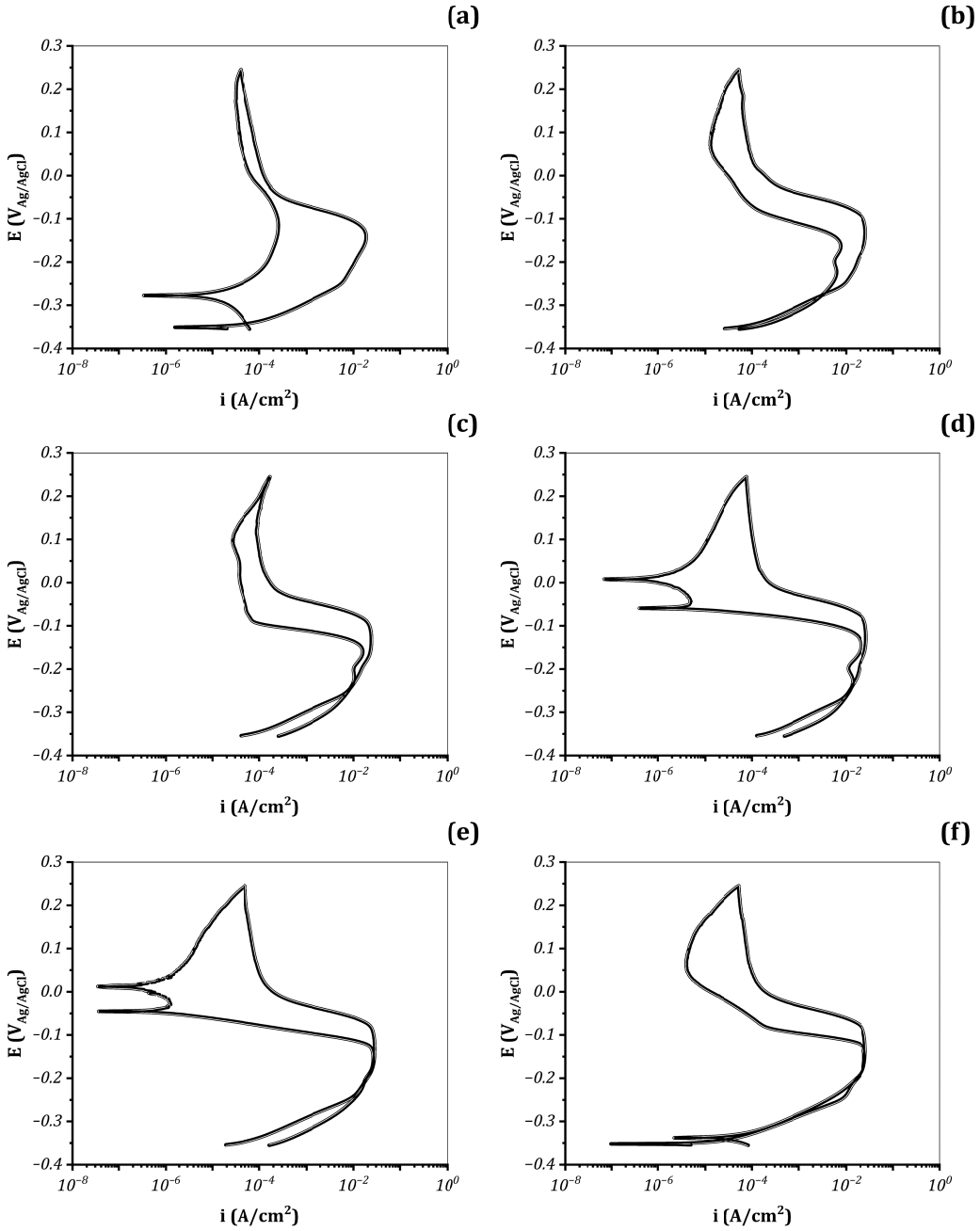

Figure 2. An outline of typical DL-EPR test profiles emanating from the unstrained DSS material in the wake of incurring the spectrum of sensitization treatments adopted in this investigative endeavor. These are namely, solution annealing at 1050 °C for half an hour followed by ageing at 850 °C for 0.0 h (**a**), 1 h (**b**), 3 h (**c**), 5 h (**d**), 8 h (**e**) and 17 h (**f**).

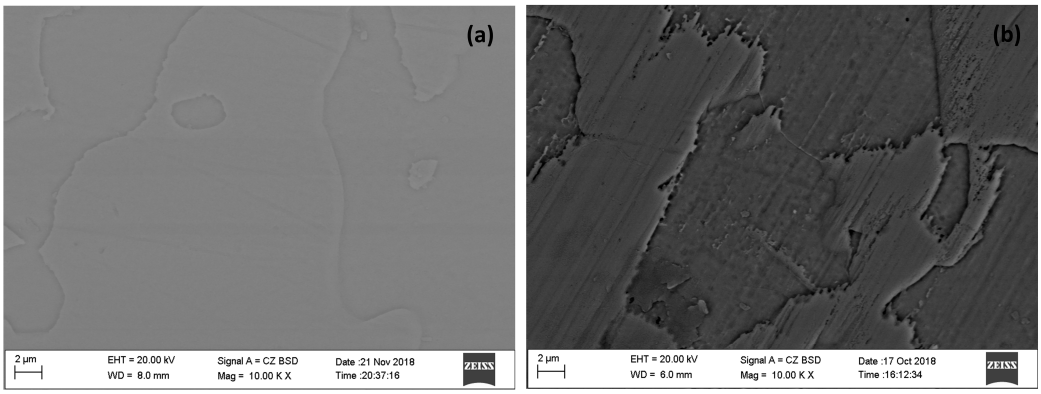

Figure 3. Scanning electron micrographs acquired in the wake of DL-EPR testing of unstrained samples, namely the solution annealed condition at 1050 °C for half an hour (**a**) and that entailing an additional sensitization treatment at 650 °C for 1 h (**b**). Micrographs of both conditions depict a mere stepped theme of microstructural detriment characteristic of non-sensitized materials.

Nonetheless, 650 °C remains relatively too low a temperature that only prolonged ageing times would warrant the triggering of an appreciable eutectoid decomposition of delta ferrite into regenerated austenite while depositing surplus chromium into the sigma phase and out of solid solution. Having said that, mild ageing times commencing at around 3 h, maybe more evidently at 5 h, would not evoke sufficient Cr-depletion adjacent to their periphery with surrounding bulk lattice to allow for the documentation of an appreciable attack, let alone pave the way for inclusion fallout, as argued for in the aforementioned—see Figure 4a,d. As a matter of fact, such inclusions are so far and few between and are relatively miniscule compared to the case of the superior 850 °C that they do not readily transpire in the midst of SAED scrutiny, which holds true for the entire spectrum of ageing times adopted for the 650 °C treatment—see Figure 5. It would not be until advanced ageing times are deployed, such as the likes of 17 h, and to a lesser extent 8 h, that a moderately blemished topographical appearance might be witnessed in the wake of a seemingly benign second-phase inclusion population fallout. All the while, this is present in synergy with a matured breadth of intergranular ditching, as indicated in Figure 4e,h. This is warranted by the fact that a discernible distinction/contrast between the two members of the twin-peak configuration in reactivation profiles at −0.15 and −0.25 V Ag/AgCl is solely succumbed to for 8 and 17 h of ageing—see Figure 1e,f.

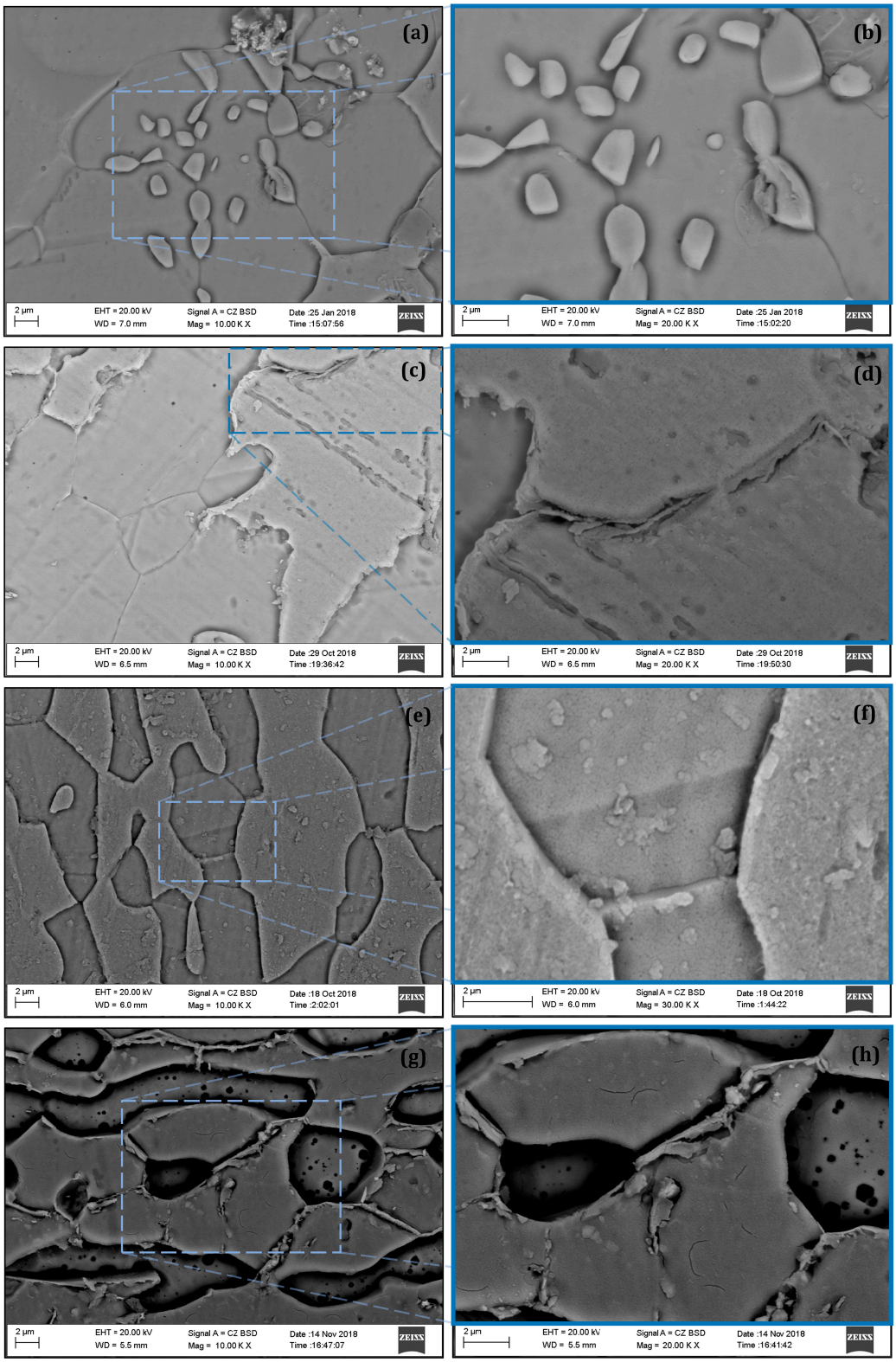

Figure 4. Scanning electron micrographs acquired in the wake of DL-EPR testing the unstrained material after having weathered solution annealing at 1050 °C for half an hour succeeded by 650 °C sensitization treatments spanning over 3 h (**a**,**b**), 5 h (**c**,**d**), 8 h (**e**,**f**) and 17 h (**g**,**h**). Micrographs on the rightmost column provide higher magnification insight on locales of interest indicated in counterpart images occupying the left column.

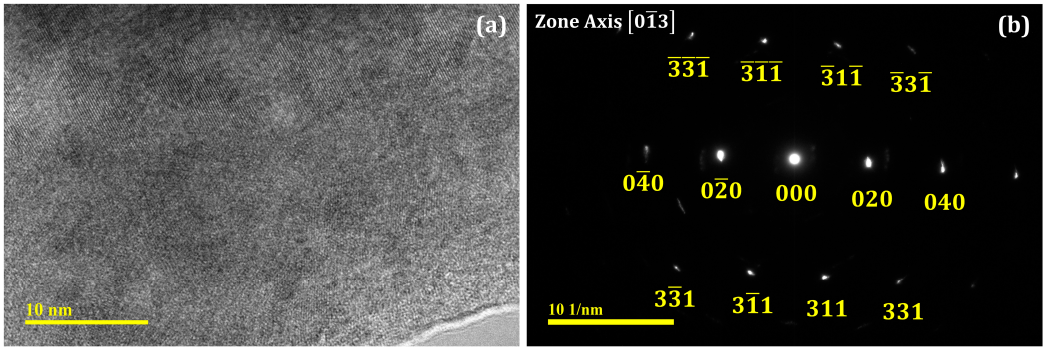

Figure 5. Transmission electron microscopy (TEM) (**a**) and selected area electron diffraction (SAED) (**b**) scrutiny of ferrite (α-Fe) locales found consistently deprived of discernable σ-phase presence across the breadth of 650 °C treated samples taken along a $[0\bar{1}3]$ zone axis. The pattern was vetted against a model for the phase in concern as proposed by Wyckoff [54] down to a d-spacing standard deviation of 2×10^{-4}.

3.2.2. Heat Treatment 2

It is by virtue of an anticipated near-entire takeover by austenitic isles against a dwindling remanence of legacy δ-ferrite presence as 850 °C is deployed [32,33] that unique occurrences tend to unfold earlier than would be foreseen with the likes of 650 °C treatments, namely those marking the dawn of microstructural features coinciding with precursor events to pronounced auxiliary peaks in DL-EPR profiles—see Figure 2b. The latter comes into fruition in association with what might otherwise be dubbed mild heat treatments. An immediate manifestation lies in the 1 h ageing treatment seeing an emergence of intragranular intermetallic second-phase precipitation known for bearing the excess chromium that surpasses the lattice capacity of the now-regenerated austenite—that is, in the wake of δ-ferrite eutectoid decomposition. The very existence of such inclusions was corroborated through a selected area electron diffraction (SAED) critique of their locales, as depicted in Figure 6 and Table 2, though the X-ray diffraction (XRD) probing also adopted had fallen short of mustering adequate resolve to pick up on the particles in concern—see Figure 7. The latter feature of XRD spectra stands reminiscent of probing attempts of the inferior 650 °C treatments, yet anticipatedly so. Worth noting is that scrutiny of SAED patterns undertaken was pursued against a model for $(Cr_{11}Fe_{13}Ni_3)Mo_3$, proposed by Hjerten et al. [55] along a low-index zone axis that is [100]. This endeavor had ultimately unveiled the culprit structure to assume lattice parameters a, b, c, α, β and γ of 8.8915 Å, 4.6088 Å, 8.8618 Å, 90°, 90.15° and 90°, respectively. This all the while entertaining Hermann–Mauguin and Hall space groups of P 121 and P 2y, correspondingly. Discernable Cr-depletion below the 16 wt% threshold concomitants to these sigma-phase inclusions was also documented (see Figure 8) in tandem with a near absence of similar depletions in the immediate adjacency to grain boundaries at such immature settings. Note that continuous intergranular ditching is not yet succumbed to at such an early stage where a stepped and granularly faceted topography seems to reign prevalent. This might be indicative of a dominant thermodynamic tendency towards dissolution exhibited by the highly energetic grain misalignment interfaces as opposed to chromium depleted locales, see Figure 9a. A broadening dispersion/dissemination of second-phase inclusions does constitute a common encounter with longer ageing times. Yet, it presides in conjunction with an onset of growingly pronounced ditching at the grain-boundary vicinity. The latter ultimately develops into a mature and consistent attack that encompasses entire grain peripheries, indicating complete sensitization stature, as evident in Figure 9b. This is because prolonged ageing beyond 1 h would bring about an enhanced thermodynamic inclination towards grain boundaries this time around as preferential microstructural features warranting attack at their locale. This occurs while overshadowing second-phase inclusions and to a larger extent grain misorientation interfaces. Such crystallographic features in coincidence with ageing times as late as 3 h are rendered relatively inferior in lattice strain energy at this stage. This turn of events

finds attestation from thereon out in the dual presence of a broadened intergranular attack perforating virtually unscathed throughout, while there is a less pronounced assault at second-phase inclusions and a vague stepping lurk in the background. Worth noting in this context is the agency of interfacial decohesion, albeit between σ-phase inclusions and adjacent matrices, δ-/δ-Fe or regenerated-γ/δ-Fe borders underpinned by residual stresses in conjunction with defect-induced stress concentration [56].

This, however, should by no means be misconstrued as suggesting a decelerated second-phase nucleation with increased ageing times. In fact, the gist of findings put forth in this investigative endeavor backed by a wealth of research argue [32,33,35] the opposite. It is rather the competing lattice strain energies amongst vulnerable features in coexistence at such extended ageing times that often designate Cr-depletion adjacent to grain boundaries as a subject worthy of selective dissolution out of all contending features.

A seemingly enhanced vulnerability towards grain fallout embarked upon by 5 h of ageing time leads to a defiled/disrupted passive film uniformity across sample surfaces, as presented in Figure 9c. This interestingly coincides with a delayed emergence of a cathodic loop being reported for the unstrained 5 h ageing time in Figure 2d, which might be attributed to 850 °C (as opposed to 650 °C) entertaining mature decomposition into the regenerated austenite. Austenite stands minutely riddled with invasive grain-boundary precipitates in the described circumstances, thereby ridding potential protective film cohesion from the infamous protrusion of such inclusions. This is as opposed to peer adjustments to cathodic reaction kinetics, recorded as early as 3 h, pertaining to the 650 °C sensitization treatment. As ageing times cross into the realm spanning between 8 and 17 h, it would seem that the severity of grain-boundary vicinity Cr-depletion had been exacerbated to such an extent that it outweighs other vulnerable crystallographic features, thereby swaying contending kinetics in its favor. Ample attestation might be found in STEM-EDX line scans conducted across three locales along a grain boundary typical of a 850 °C 17 h sensitized specimen, in which the latter exhibited Cr-depletions that encroach upon the threshold marking the onset of vulnerability towards IGC and worthiness of being dubbed active, namely 16 wt% Cr [7,8,57–59]—see Figure 10. Figure 9d,e documents dwindling relics of intragranular second-phase presence whilst being dwarfed by rigorous grain-boundary ditching. Furthermore, the sole successful attempt at probing the vicinity of the already-scarce sigma-phase presence had fallen short of documenting any significant Cr-depletions in immediate adjacency to the latter below bulk concentrations, as is depicted in Figure 11. All in all, the collective gist of findings amassed might also find corroboration if one would recall that reverse peaks were leveraged predominantly by corrosion currents stemming from metal dissolution at grain-boundary locales whilst completely diminishing auxiliary peaks attributed to second-phase contribution that formerly resided at −0.25 V Ag/AgCl—see Figure 2e,f [33].

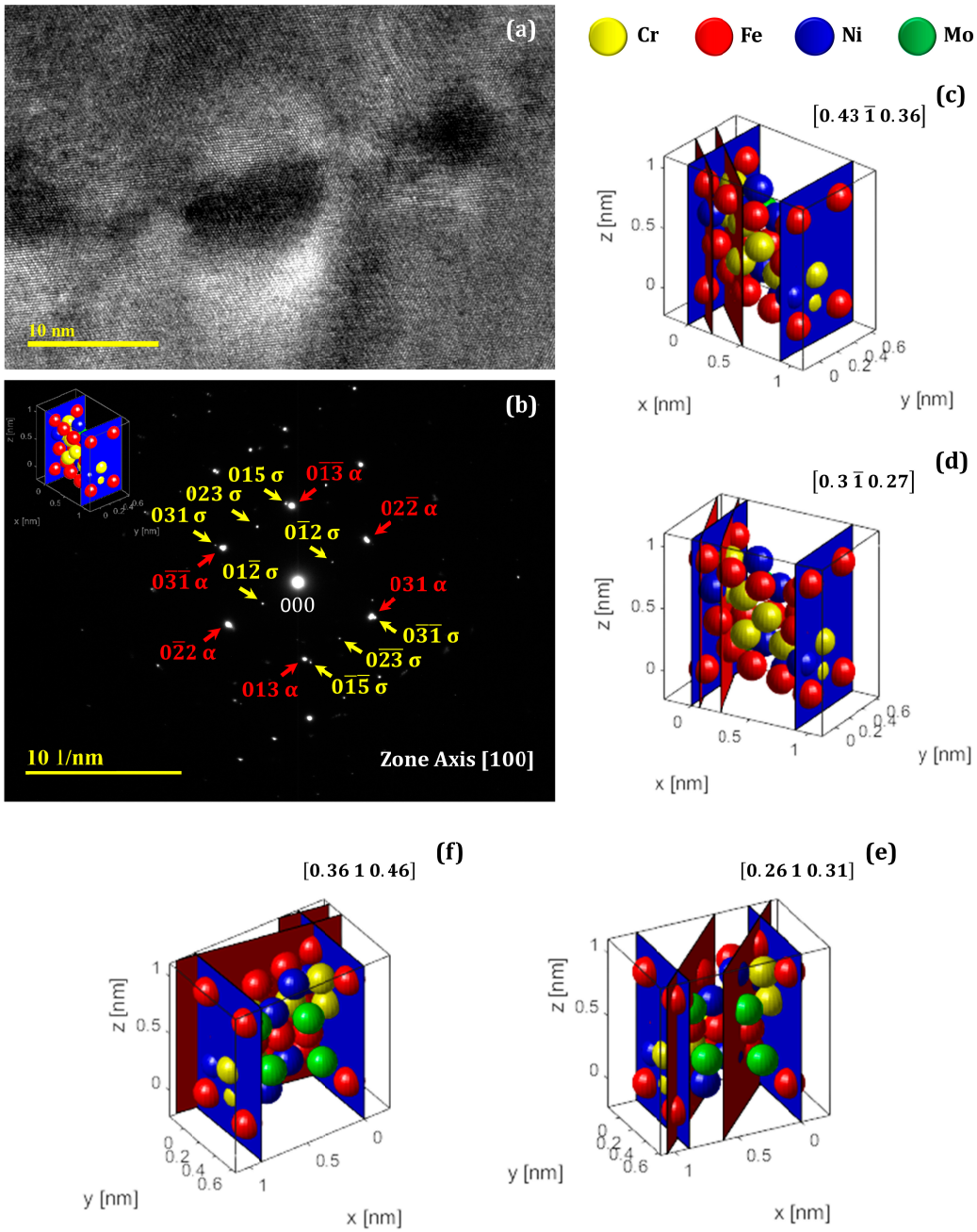

Figure 6. Ascertained presence of sigma phase dispersed amongst a matrix of ferrite (α-Fe) by way of transmission electron micrographic (TEM) attestation (**a**), vetting of selected area electron diffraction (SAED) against a model for $(Cr_{11}Fe_{13}Ni_3)Mo_3$ as proposed by Hjerten et al. [55] discernable along a low-index zone axis of [100] yielding a d-spacing standard deviation that amounts to 9×10^{-4} (inset figure showcases the 3D rendition of pertinence to the model in concern with planes normal to zone axis indicated) (**b**). The relative orientations of candidate planes—as per the model—and that normal to the zone axis are depicted as 52.13° for (320) (**c**), 21.1° for (510) (**d**), 43.97° for $(2\bar{1}0)$ (**e**) and 99.8° for $(\bar{1}30)$. Bravais indices discernable on top-right corners of figures (**c**–**f**) correspond to real-time zone axes of each 3D perspective discretely.

Table 2. Description of phases indexed amid SAED and XRD pattern scrutiny.

	Ferrite (α-Fe)		**Austenite (γ-Fe)**		**σ Phase**	
Chemical Formula	Cr Fe		C Fe		$Cr_{11}Fe_{13}Ni_3Mo_3$	
Crystal Structure	BCC		FCC		Monoclinic	
Lattice Parameters:						
a	2.8665 Å		3.5950 Å		8.8915 Å	
b	2.8665 Å		3.5950 Å		4.6088 Å	
c	2.8665 Å		3.5950 Å		8.8618 Å	
α	90°		90°		90°	
β	90°		90°		90.15°	
γ	90°		90°		90°	
Cell Volume	23.554 $Å^3$		46.462 $Å^3$		363.148 $Å^3$	
Space Group Designation:						
Hermann–Mauguin	I m $\bar{3}$ m		F m $\bar{3}$ m		P 1 2 1	
Hall	$\bar{I}$ 4 2 3		$\bar{F}$ 4 2 3		P 2y	
Zone Axis	[100]		[1$\bar{3}$0]		[100]	
Planes Identified	Miller Indices	d-spacing (1/nm)	Miller Indices	d-spacing (1/nm)	Miller Indices	d-spacing (1/nm)
	(022)	4.479	(311)	9.6448	(023)	4.4788
	(013)	4.952	(313)	12.6928	(015)	4.9518
	(0$\bar{1}$1)	2.614	(002)	5.8703	(0$\bar{1}$2)	2.6144
	(0$\bar{3}$1)	5.410	($\bar{3}$11)	9.688	(0$\bar{3}$1)	5.4102
d-spacing Std Dev	0.0097		0.0002		0.0009	
Source Model	Wyckoff [54], Andersen et al. [60], Badjuk et al. [61], Dorofeev et al. [62]		Nishihara et al. [63], Oila et al. [64], Goldschmidt [65]		Hjerten et al. [55], Yakel [66], Bergman et al. [67]	

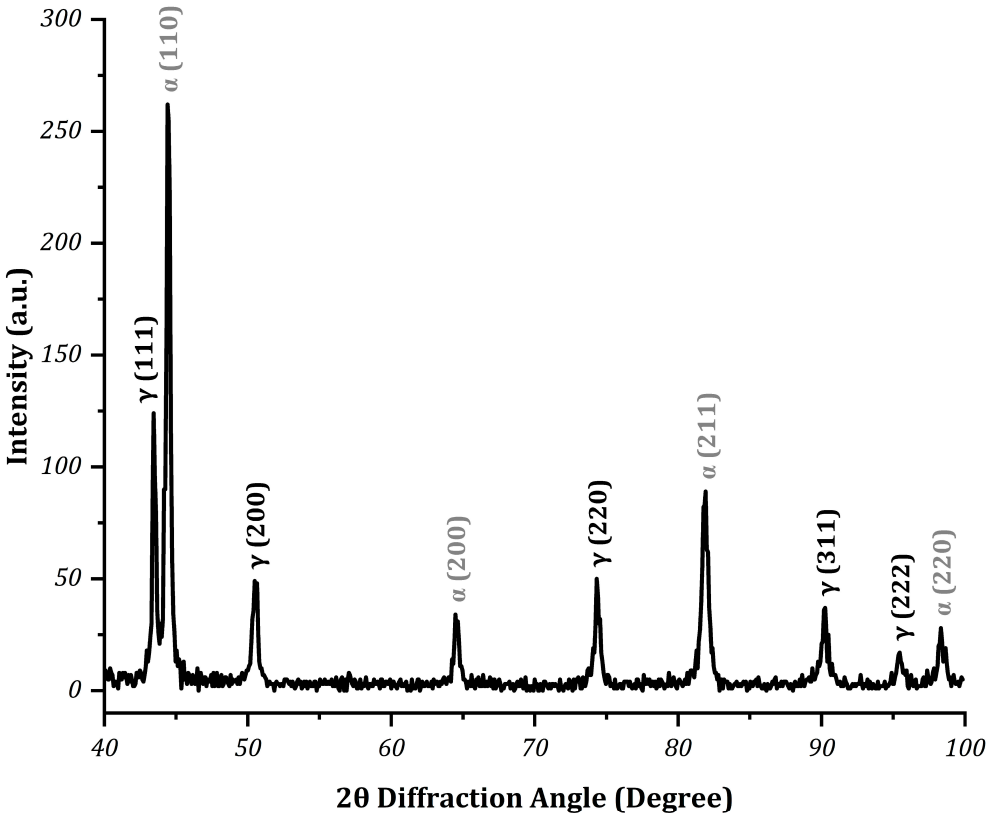

Figure 7. X-ray Diffraction (XRD) pattern scrutiny of the very condition, namely 850 °C for 3 h, probed via Selective Area Electron Diffraction (SAED) in Figure 6 faring triumphant in detecting the duo of ferrite (grey) and austenite (black) phases [65,68] yet falling short of mustering adequate resolve to pick up on sigma phase.

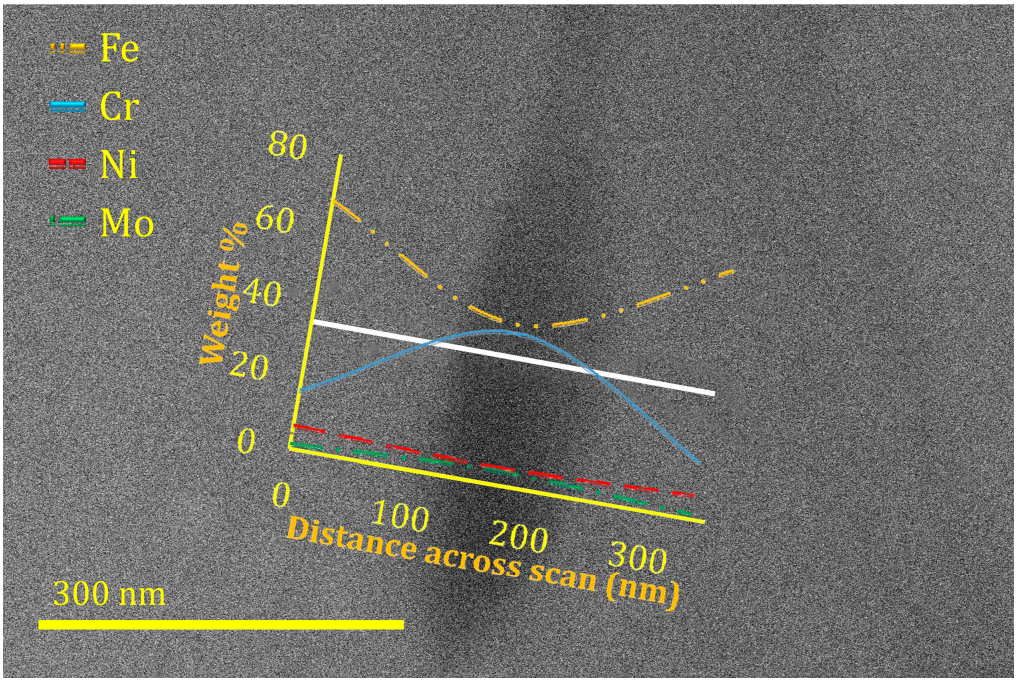

Figure 8. A STEM-EDX line scan (in white) administered across a sigma-phase inclusion depicting (wt%) profiles for Fe, Cr, Ni and Mo characteristic of the shorter ageing times at 850 °C (namely, the 1-h variant) that exhibit pronounced Cr-depletion in the immediate vicinity to such inclusions.

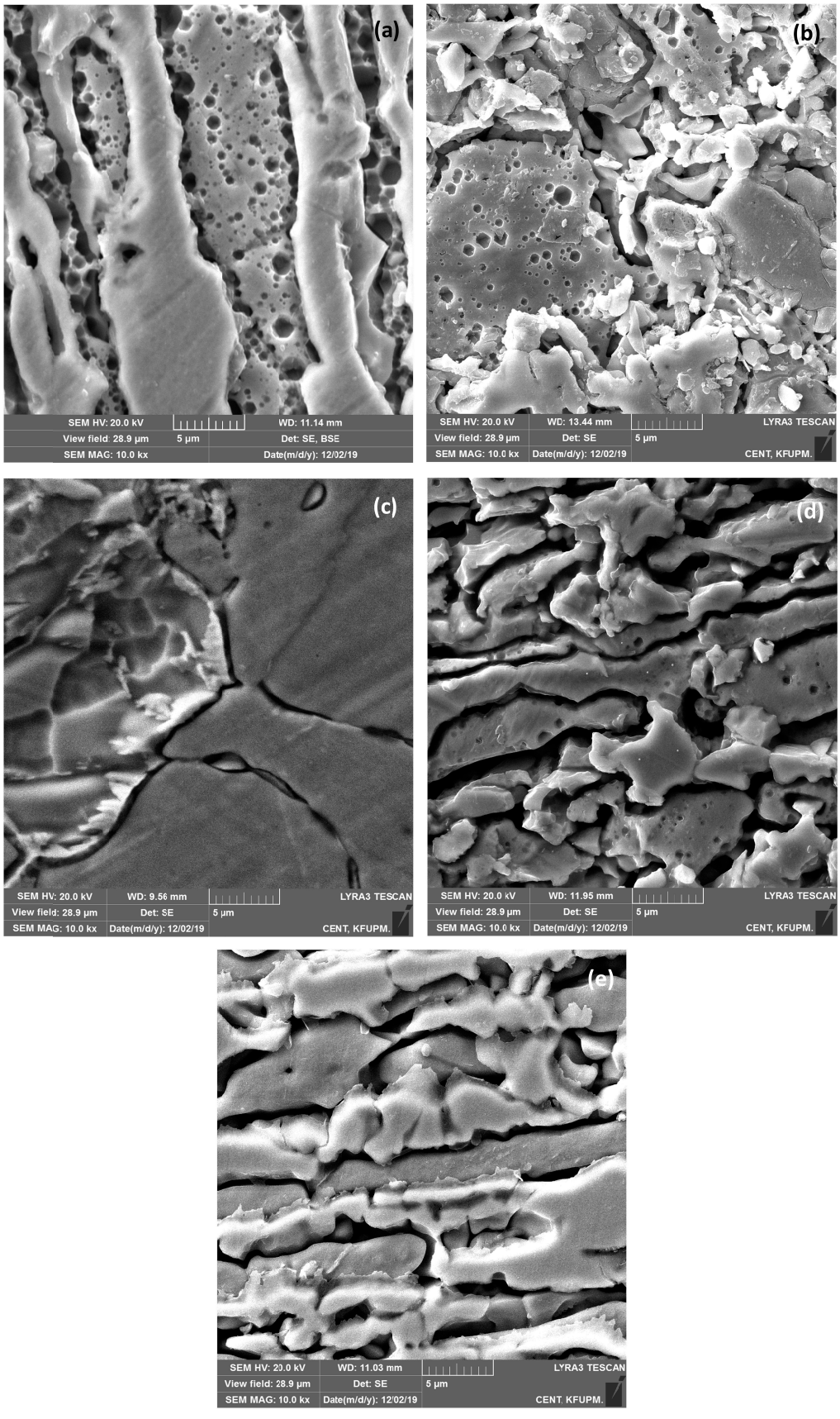

Figure 9. Scanning electron micrographs acquired in the wake of DL-EPR testing the unstrained condition after having endured solution annealing at 1050 °C for half an hour followed by sensitization at 850 °C for 1 h (**a**), 3 h (**b**), 5 h (**c**), 8 h (**d**) and 17 h (**e**).

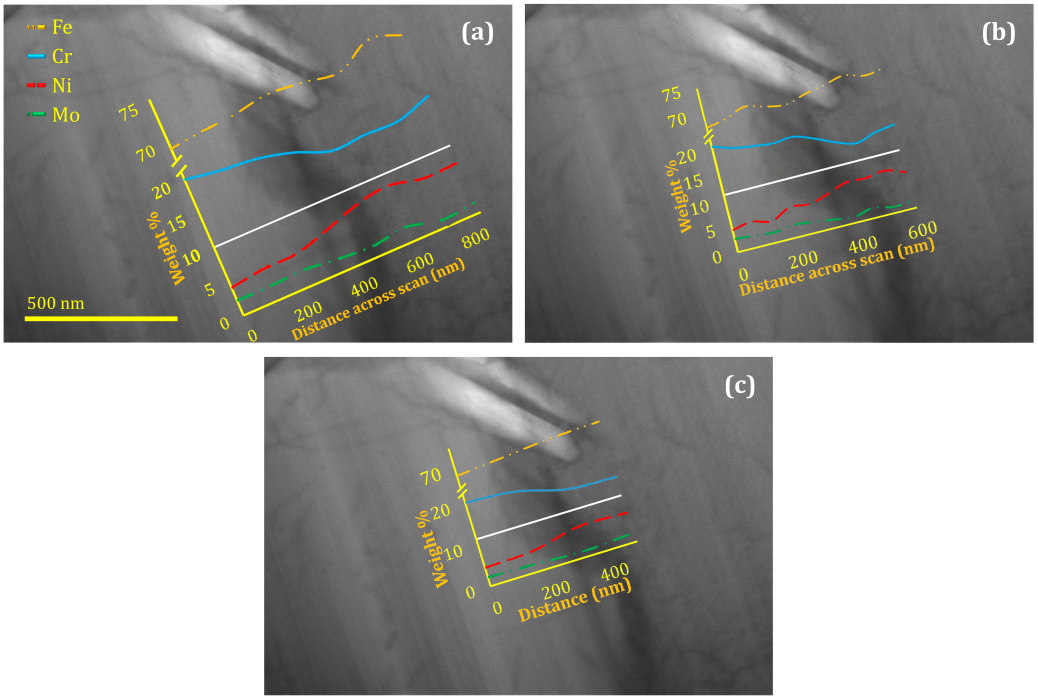

Figure 10. Three (**a**–**c**) STEM-EDX line scans (in white) conducted across discrete locales along a grain boundary typical of the 850 °C 17 h condition depicting Fe, Cr, Ni and Mo microconstituent profiles in wt%.

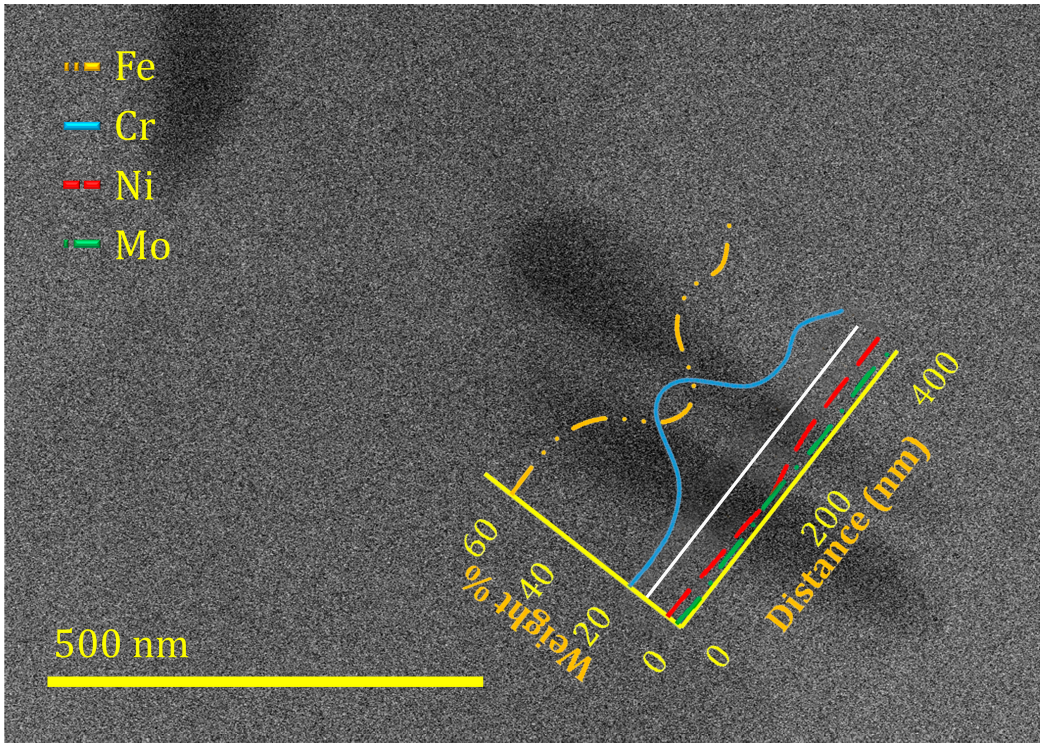

Figure 11. A STEM-EDX line scan (in white) administered across a remnant sigma-phase inclusion depicting (wt%) profiles for Fe, Cr, Ni and Mo characteristic of the 850 °C 17 h condition that are deprived of significant deviation from matrix concentrations along the periphery of such inclusions.

3.3. Normalized Perspective on DL-EPR Data

A more meticulous grain-size-advised take on handling the raw ir/ia data initially presented in Section 3.1 is being put forth here. This is realized through the normalization of

crude data in accordance with the Cihal method [6,19–21] before ultimately complementing the mere averaged perspective offered by the latter, with precise renditions predicated upon an actual boundary-by-boundary subjective dimensional critique. This is facilitated by deploying the image segmentation feature in Matlab. The scheme for the so-called normalization endeavors undertaken here was bifrontal in nature, as it was sought whilst accounting for length and effective surface area of grain-boundary networks each discretely.

3.3.1. Heat Treatment 1

The thorough probing of Figure 12a,b yields a mutual inference pertaining to the breakaway in plain i_r/i_a that resides in the vicinity of 8 h ageing time—a trend that is intimately mimicked by profiles of the Cihal-normalized DoS, which manifests in the departure from a plateau that shies from the 0.05 i_r/i_a mark as the threshold of 8 h ageing time is breached, where the 0.05 i_r/i_a datum line confines the realm of mild sensitization lying underneath. This trend, anticipatedly, holds true for GBL and GBA predicated profiles of normalized DoSs alike. Yet, inevitably, the Cihal-normalization profile does eventually trace a path that winds up nearly double that of plain i_r/i_a since the onset of their divergence. This transpires in the amplification of values that used to reside typically at 0.024 $\pm$ 0.0183 and 0.246 $\pm$ 0.0398 for the 8 and 17 h conditions, respectively, and of plain i_r/i_a into 0.053 $\pm$ 0.0084 and 0.590 $\pm$ 0.1409 for the 8 and 17 h conditions, respectively, once Cihal normalization was deployed.

Image processing, however, unveils a point that marks premature DoS breakaway in adjacency to 5 h ageing time—an observation that stands indifferent to whether GBL or GBA predicated normalizations are at stake. It is nonetheless discernible that the GBA-based normalization indulges typical i_r/i_a values that flirt with the threshold marking considerable sensitization hovering around 0.05—that is, prior to giving in to an inclination to ascend towards values of 0.076 $\pm$ 0.0273, and 0.196 $\pm$ 0.0194 for 5 and 8 h, respectively, and ultimately soaring as high as 1.234 $\pm$ 0.2449 by 17 h ageing time. In doing so, the image processing-normalized DoS would have risen nearly an additional twofold over its Cihal-normalized counterpart by 17 h. Though, it might be granted that the restricted number of measurements of grain-boundary width somewhat depreciates the accuracy of the GBL predicated approach in offering a statistically sound inference on DoS. Where the latter might otherwise stand to rise to the level of GBA normalized counterparts. GBL normalization, nonetheless, does put forth a depiction of DoS which is not that far removed from its more precise peer.

The breadth of attempts exhibited across the board, irrespective of their approach on normalization, had attested to the notorious insensitivity of DL-EPR towards overwhelming DoS brought about by protracted ageing times, the likes of 17 h. This might be found demonstrated in the broadening of experimental scatter signaling a marked inconsistency in i_r/i_a measurements within the realm of ageing time in concern.

3.3.2. Heat Treatment 2

A telling display of transition amongst the successive milestones documented in microstructural evolution that had to be weathered by the material with growing ageing time at 850 °C might be seen faithfully corroborated in Figure 13. This is especially pronounced in tracking the profile for the DoS intricate divulgation approach predicated upon image processing that is particularly GBA-based. An isolated critique of the latter documents an abrupt breakaway in i_r/i_a readily materializing in coincidence with 1 h ageing time where DoS somewhat plateaus at a value marking severe detriment of near unity leading up to 3 h of ageing time. Note that such a breakaway proves reminiscent of the reactivation kinetics resurgence documented at such an early stage (namely, 1 h) for 850 °C, see Figure 2a,c, attributed at the time to pronounced sigma-phase fallout documented in Figure 9a,b, see Sections 3.1.2 and 3.2.2.

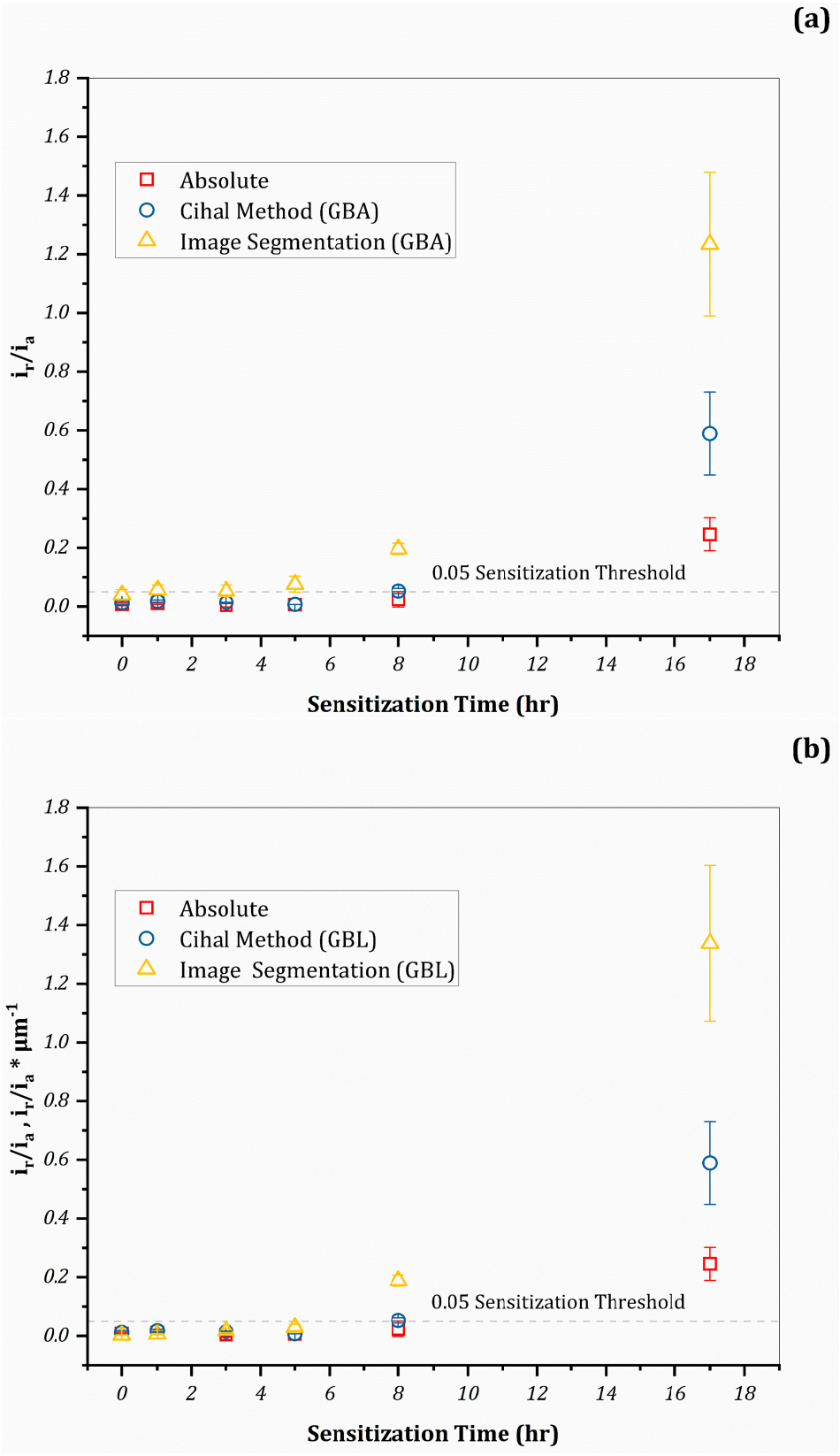

Figure 12. Cross-comparison of DoS with emphasis on breakaway thresholds characteristic of conventional and normalized DL-EPR predicated upon grain-boundary physical dimensions. DoS presented are for the spectrum of ageing times adopted in this study pertaining to the 650 °C sensitized material. Depictions showcased are of GBA- (**a**) and GBL- (**b**) normalized renditions vs. conventional i_r/i_a, where error bars represent standard deviation span of nine discrete measurements.

The i_r/i_a profile soon departs from its former state of stagnation (or dwelling) on the approach to 5 h of ageing time. Where this pivotal point in microstructural evolution stands reminiscent of evidenced depreciation of passive film coherence (Figure 9c) in coincidence with the dawn of cathodic loops in the midst of DL-EPR testing, see Figure 2d,e. The profile eventually succumbs to an inferiorly steep ascend with the onset of 8 through to 17 h of ageing time. This is as the kinetics of reverse-current detriment are overtaken by a newfound thermodynamic tendency towards dissolving a mature chromium depleted microchemistry generated at grain-boundary adjacency that eclipses any remnants of competition imposed by sigma-phase locales. A phenomenon that is documented in the waning of twin reverse-scan peaking or 'i_r' resurgence in coincidence with 8 and 17 h (Figure 2e,f). Which translates undeniably in an absence of any signs of sigma-phase fallout on postmortem sample surfaces. This all the while being reported in conjunction with prominent intergranular attack propagation and broadening, see Figure 9e.

Key takeaways drawn from Figure 13 might be found accentuated in Table 3, which attests to an all-encompassing theme, whether GBA or GBL normalizations are in concern. This manifests in the reported tendency towards the surpassing of the threshold that confines benign DoS (conventionally set at 0.05) in embarking upon ageing times as miniscule as 1 h. Yet the image processing-normalized variant seems to exceed both the plain and Cihal-normalized counterparts by a near 2.2- and 1.4-times, for the GBA- and GBL-based normalizations, respectively. This is because the latter two reside virtually within experimental scatter of each other.

Table 3. Analysis of key findings depicted in Figure 13 highlighting the superiority of image processing predicated upon the GBA normalization in accurate and consistent prediction of DoS as opposed to other variants.

	Average GBA-Normalized 'i_r/i_a'			**Average GBL-Normalized 'i_r/i_a'**			**% Error Relative to 'Exact' GBA-Based Approach** $\left(\frac{IP_{GBA}-IP_{GBL}}{IP_{GBA}}\right)\times 100$
Heat Treatment	**Cihal Method (CM)**	**Image Processing (IP)**	**IP/CM Advantage**	**Cihal Method (CM)**	**Image Processing (IP)**	**IP/CM Advantage**	
Ref	0.0195 ±0.0003	0.0436 ±0.0009	~2.24 times	0.0195 ±0.0003	0.0129 ±0.0003	~0.66 times	70.41
1 h	0.4611 ±0.0527	1.0182 ±0.1227	~2.21 times	0.4611 ±0.0527	0.6547 ±0.0789	~1.42 times	35.70
3 h	0.6195 ±0.1371	1.1809 ±0.261	~1.91 times	0.6195 ±0.1371	0.9435 ±0.2085	~1.52 times	20.10
5 h	0.8111 ±0.0815	1.8322 ±0.1933	~2.26 times	0.8111 ±0.0815	1.7515 ±0.1848	~2.16 times	4.40
i_r/i_a Breakaway							
8 h	1.4363 ±0.0231	2.75 ±0.076	~1.91 times	1.4363 ±0.0231	2.7528 ±0.076	~1.92 times	−0.10
17 h	1.6985 ±0.2836	4.4744 ±0.3642	~2.63 times	1.6985 ±0.2836	6.1747 ±0.5026	~3.64 times	−38.0

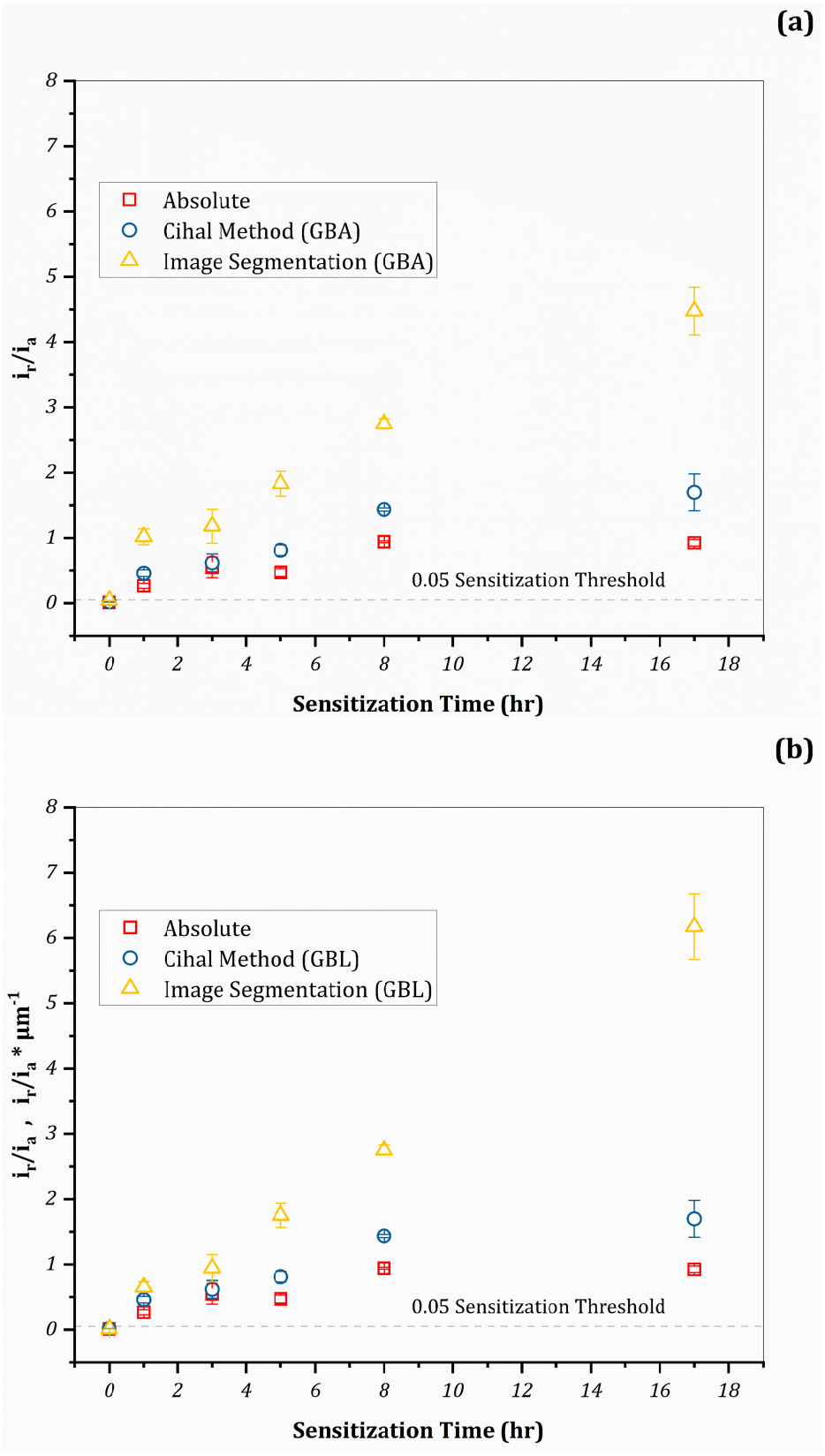

Figure 13. Cross-comparison of DoS with emphasis on breakaway thresholds characteristic of conventional and normalized DL-EPR predicated upon grain-boundary physical dimensions. DoS presented are for the spectrum of ageing times adopted in this study pertaining to the 850 °C sensitized material. Depictions showcased are of GBA- (**a**) and GBL- (**b**) normalized renditions vs. conventional i_r/i_a, where error bars represent standard deviation span of nine discrete measurements.

As profiles of the two normalization variants are shown to part ways, the honor of most significant divergence rests in the court of the image processing-affiliated approach. This is owing to the fact that the Cihal normalization only offsets the plain i_r/i_a profile by an average of 1.7 times from thereon out. Meanwhile, the image processing approach (irrespective of whether GBA- or GBL-based) appears to have towered over its Cihal-normalized counterpart by approximately 2.2 and 1.9 times for 5 and 8 h, respectively. This is before the two methods diverge yet again, as attempts predicated upon GBA normalization yield a near 2.6-fold advantage, while their GBL-based peers surpass that around 3.6 times. The rationale for the latter discrepancy and emergence of broadened experimental scatter in coincidence with the 17 h ageing time, particularly in the context of GBL normalization, was elaborated on in earlier sections.

All in all, the overriding gist of findings exhibited here serves in further corroborating the superiority of image processing-aided normalizations as opposed to their Cihal method-based counterparts. This ascendancy was perceived as being further strengthened when normalizations predicated upon GBA are pursued rather than their GBL-based peers—that is, in as far as an accurate and consistent prediction of DoS is concerned.

4. Conclusions

- The 650 °C treatment appeared to promote an incomplete ferrite eutectoid decomposition compared to the 850 °C treatment. At 650 °C, sigma-phase precipitation was delayed, occurring after 3 h of aging, as observed through reactivation kinetics and SEM analysis. However, significant dissolution and a limited fallout of features occurred only after 8 h of aging, contrasting with the rapid sigma-phase fallout observed at 850 °C after just 1 h of aging. Additionally, an early onset of reverse-current twin peaking was observed at 850 °C.
- The aforementioned was attributed to the rendering into existence of Cr-depletions that descend below a threshold of 16 wt% in close vicinity to sigma-phase inclusions solely characteristic of miniscule ageing times adopted for the 850 °C treatment. This is in addition to the grain-boundary adjacency that is riddled with an identical fate in the wake of protracted ageing times being adopted for both the 650 °C and 850 °C treatments.
- Anticipatedly, an abrupt breakaway in i_r/i_a had only come into fruition after a weathering 8 h of ageing at 650 °C—an event that was reeled in towards a premature stature of 1 h with the 850 °C treatment.
- Efforts invested in formulating a fair depiction of the DoS through normalization attempts predicated upon grain-boundary physical dimensions (vis-à-vis GBA and GBL) exhibited a near-consistent leaning towards doubling i_r/i_a values progressively in the following sequence: plain i_r/i_a, Cihal- and then IP-normalized by 17 h of ageing time. There was a distinct premature breakaway in i_r/i_a at 5 h for IP-normalized as opposed to 8 h of ageing time typical of Cihal-normalized and plain 850 °C renditions of the 650 °C treatment.
- That is, all the while, the 850 °C condition weathers an abrupt surge of sorts, yet this is as early as 1 hr of ageing time regardless of whether absolute or normalized signals are concerned. This upsurge might be linked to the onset of sigma-phase fallout in coincidence with such a treatment.
- These observations hold true across the board for GBA- and GBL-based normalizations, yet the GBL approach remains gravely prone to experimental inaccuracies, particularly once the realm of protracted ageing times is encroached upon, where DL-EPRT is notoriously rendered insensitive to an exacerbated DoS.
- Of the constituents comprising the bifrontal scheme adopted to normalize the DoS response emerges the IP-predicated approach (particular, whilst being GBA-oriented) as a superior alternative over the Cihal method-based variant in as far as fulfilling the sought-after merits of accuracy and reproducibility.

- Ultimately, a bi-pronged approach towards DL-EPR output normalization (namely the Cihal method and image processing) was deployed with an eye on the dimensional nuance (referring to GBA and GBL) assumed by realms of attack in grain-boundary and σ-phase adjacency. Though this scheme was constructed with the intention of catering to thermal sensitization afflicting stainless steels, it might easily be expanded into addressing processes leading to similar microstructures of detriment; in Ni-Fe-Cr alloys, such as Incoloys.

Author Contributions: Conceptualization, A.F.A.; methodology, H.M.E., A.F.A. and A.S.H.; validation, A.F.A. and H.M.E.; formal analysis, A.B., H.D.M. and A.M.; investigation, A.F.A., A.B. and H.M.E.; data curation, R.R.A., M.K.A.R., A.I.R., F.A.J. and K.S.B.; writing—original draft preparation, A.F.A.; writing—review and editing, A.F.A. and H.M.E. All authors have read and agreed to the published version of the manuscript.

Funding: This research received no external funding.

Data Availability Statement: The raw data supporting the conclusions of this article will be made available by the authors on request.

Acknowledgments: The authors, expressly, wish to extend their gratitude for the efforts exerted by King Fahd University for Petroleum and Minerals through the center for Hydrogen Technologies and Carbon Management (IRC-HTCM), spearheaded by Zain H. Yamani, Abbas S. Hakeem and Hatim D. Mohamed in technically aiding the investigative work put forth.

Conflicts of Interest: The authors declare no conflicts of interest.

References

1. Pednekar, S.; Smialowska, S. The effect of prior cold work on the degree of sensitization in type 304 SS. *Corrosion* **1980**, *36*, 565–577. [CrossRef]
2. *ASTM A262-15*; Standard Practices for Detecting Susceptibility to Intergranular Attack in Austenitic Stainless Steels. ASTM International: West Conshohocken, PA, USA, 2021.
3. Devine, T.M. The mechanism of sensitization of austenitic stainless steels. *Corros. Sci.* **1990**, *30*, 135–151. [CrossRef]
4. Devine, T.M. Kinetics of sensitization and desensitization. *Acta Mater.* **1998**, *36*, 1491–1501. [CrossRef]
5. Frankenthal, R.P.; Pickering, H.W. Intergranular corrosion of ferritic stainless steel. *J. Electrochem. Soc.* **1973**, *120*, 24–26. [CrossRef]
6. *ASTM G108-94*; Standard Test Method for Electrochemical Reactivation (EPR) for Detecting Sensitization of AISI Type 304 and 304L Stainless Steels. ASTM International: West Conshohocken, PA, USA, 2015.
7. Al-Shater, A.; Engelberg, D.; Lyon, S.; Donohoe, C.; Walters, S.; Whillock, G.; Sherry, A. Characterization of the stress corrosion cracking behavior of thermally sensitized 20Cr-25Ni stainless steel in a simulated cooling pond environment. *J. Nucl. Sci. Technol.* **2017**, *54*, 742–751. [CrossRef]
8. Al-Shater, A. Intergranular Corrosion of Sensitized 20Cr-25Ni-Nb Stainless Steel Nuclear Fuel Cladding Materials. Ph.D. Dissertation, University of Manchester, Manchester, UK, 2010; p. 197.
9. Majidi, A.P.; Streicher, M.A. The Double Loop Reactivation Method for Detecting Sensitization in AISI 304 Stainless Steels. *Corrosion* **1984**, *40*, 584–593. [CrossRef]
10. Parvathavarthini, N.; Kamachi Mudali, U. Electrochemical techniques for estimating the degree of sensitization in austenitic stainless steels. *Corros. Rev.* **2014**, *32*, 183–225. [CrossRef]
11. Osozawa, K.; Bohnenkamp, K.; Engel, H.J. Potentiostatic study on the intergranular corrosion of an austenitic chromium-nickel stainless steel. *Corros. Sci.* **1966**, *6*, 421–433. [CrossRef]
12. Payer, J.H.; Staehle, R.W. The dissolution behaviour of $Cr_{23}C_6$ and TiC related to stainless steel in which they occur. *Corrosion* **1975**, *31*, 30–36. [CrossRef]
13. Altonen, P.; Aho Mantila, I.; Hannien, H. Electrochemical methods for testing the IGC susceptibility of stainless steel. *Corros. Sci.* **1983**, *23*, 431–440. [CrossRef]
14. Chung, P.; Szklarska-Smialowska, S. The effect of heat treatment on the degree of sensitization of type 304 stainless steel. *Corrosion* **1981**, *37*, 39–50. [CrossRef]
15. Clarke, W.L.; Cowan, R.L.; Walker, W.L. *Intergranular Corrosion of Stainless Alloys*; ASTM Special Technical Publication 656; ASTM: West Conshohocken, PA, USA, 1978.
16. Clarke, W.L. The EPR method for the detection of sensitization in stainless steel. In *Countermeasures for Pipe Cracking in BWRs*; Electric Power Research Institute: Palo Alto, CA, USA, 1981.
17. Akashi, M.; Kawamoto, T.; Umemura, F. Evaluation of IGSCC susceptibility of austenitic stainless steels using electrochemical reactivation method. *Corros. Eng.* **1980**, *29*, 163–169.

18. Majidi, A.P.; Streicher, M.A. Four nondestructive electrochemical tests for detecting sensitization in type 304 and 304L stainless steels. *Nucl. Technol.* **1986**, *75*, 356–369. [CrossRef]
19. *ASTM E112-24*; Standard Test Methods for Determining Average Grain Size. ASTM International: West Conshohocken, PA, USA, 2024.
20. *BS EN ISO 643:2019*; Steels—Micrographic Determination of the Apparent Grain Size. BSI Standards Publication: London, UK, 2019.
21. *ISO 12732:2006*; Corrosion of Metals and Alloys—Electrochemical Potentiokinetic Reactivation Measurement Using the Double Loop Method (Based on Cihal's Method). International Organization for Standardization: Geneva, Switzerland, 2006.
22. Bruemmer, S.M.; Was, G.S. Microstructural and microchemical mechanisms controlling intergranular stress corrosion cracking in light-water-reactor systems. *J. Nucl. Mater.* **1994**, *216*, 348–363. [CrossRef]
23. Ortner, S.R.; Randle, V. A study of the relation between grain boundary type and sensitization in a partially sensitized AISI 304 stainless steel using electron back-scattering patterns. *Scr. Metall. Metarialia* **1989**, *23*, 1903–1908. [CrossRef]
24. Shimada, M.; Kokawa, H.; Wang, Z.J.; Sato, Y.S.; Karibe, I. Optimization of grain boundary character distribution for intergranular corrosion resistant 304 stainless steel by twin induced grain boundary engineering. *Acta Mater.* **2002**, *50*, 2331–2341. [CrossRef]
25. Zhou, Y.; Aust, K.T.; Erb, U.; Palumbo, G. Effects of grain boundary structure on carbide precipitation in 304L stainless steel. *Scr. Mater.* **2001**, *45*, 49–54. [CrossRef]
26. Rahimi, S.; Engelberg, D.L.; Duff, J.A.; Marrow, T.J. In situ observation of intergranular crack nucleation in a grain boundary controlled austenitic stainless steel. *J. Microsc.* **2009**, *233*, 423–431. [CrossRef] [PubMed]
27. Rahimi, S.; Engelberg, D.L.; Marrow, T.J. Characterisation of grain boundary cluster compactness in an austenitic stainless steel. *J. Mater. Sci. Technol.* **2010**, *26*, 670–675. [CrossRef]
28. Rahimi, S.; Engelberg, D.L.; Marrow, T.J. Characterisation of the sensitization behaviour of thermomechanically processed type 304 stainless steel using DL-EPR testing and image analysis methods. In Proceedings of the 2nd International Conference, Corrosion and Material Protection, Prague, Czech Republic, 19–22 April 2010.
29. Rahimi, S.; Engelberg, D.L.; Marrow, T.J. A new approach for DL-EPR testing of thermo-mechanically processed austenitic stainless steel. *Corros. Sci.* **2011**, *53*, 4213–4222. [CrossRef]
30. Rahimi, S.; Marrow, T.J. A new method for predicting susceptibility of austenitic stainless steels to intergranular stress corrosion cracking. *Mater. Des.* **2020**, *187*, 108368. [CrossRef]
31. Kain, V.; Prasad, R.C.; De, P.K. Detection of sensitization and intergranular corrosion of Fe-Cr-Ni alloys. *High Temp. Mater. Process.* **1997**, *16*, 183–200. [CrossRef]
32. Warren, A.D.; Harniman, R.L.; Guo, Z.; Younes, C.M.; Flewitt, P.E. Quantification of sigma-phase evolution in thermally aged 2205 duplex stainless steel. *J. Mater. Sci.* **2016**, *51*, 694–707. [CrossRef]
33. Amadou, T.; Braham, C.; Sidhom, H. Double Loop Electrochemical Potentiokinetic Reactivation Test Optimization in Checking of Duplex Stainless Steel Intergranular Corrosion Susceptibility. *Metall. Mater. Trans. A* **2004**, *35*, 3499–3513. [CrossRef]
34. Wang, R.; Imagawa, M.; Honda, M.; Mori, T.; Fukuhara, H. Double-loop electrochemical potentiokinetic reactivation behaviour of continuously cooled SUS329J4L duplex stainless steel. *Corros. Eng. Sci. Technol.* **2018**, *53*, 44–50. [CrossRef]
35. Arıkan, M.E.; Arıkan, R.; Doruk, M. Determination of Susceptibility to Intergranular Corrosion of UNS 31803 Type Duplex Stainless Steel by Electrochemical Reactivation Method: A Comparative Study. *Int. J. Corros.* **2012**, *2012*, 478508. [CrossRef]
36. Wang, R.; Imagawa, M.; Honda, M.; Fukuhara, H. Single Loop Electrochemical Potentiokinetic Reactivation Behaviour of Continuously Cooled SUS329J4L Duplex Stainless Steel. *Int. J. Mech. Syst. Eng.* **2017**, *3*, 125. [CrossRef] [PubMed]
37. Zinkle, S.J.; Was, G.S. Materials challenges in nuclear energy. *Acta Mater.* **2013**, *61*, 735–758. [CrossRef]
38. Fan, Y.; Liu, T.G.; Xin, L.; Han, Y.M.; Lu, Y.H.; Shoji, T. Thermal aging behaviors of duplex stainless steels used in nuclear power plant: A review. *J. Nucl. Mater.* **2021**, *544*, 152693. [CrossRef]
39. *IAEA-TECDOC-1557*; Assessment and Management of Ageing of Major Nuclear Power Plant Components Important to Safety: PWR Vessel Internals. International Atomic Energy Agency (IAEA): Vienna, Austria, 2007.
40. *NEA/CSNI/R(2002)26*; Technical Aspects of Ageing for Long-Term Operation. Committee on The Safety of Nuclear Installations: Paris, France; Nuclear Energy Agency (NEA): Singapore; Organization for Economic Cooperation and Development (OECD): Paris, France, 2003.
41. Li, C.; Zhu, J.; Cai, A.; Mei, L.; Jiao, X.; Du, X.; Wang, K. Microstructure and Corrosion Resistance of Underwater Laser Cladded Duplex Stainless-Steel Coating after Underwater Laser Remelting Processing. *Materials* **2021**, *14*, 4965. [CrossRef]
42. Lo, K.H.; Shek, C.H.; Lai, J.K. Recent developments in stainless steels. *Mater. Sci. Eng. R* **2009**, *65*, 39–104. [CrossRef]
43. Erdman, N.; Bell, D.C.; Reichelt, R. Scanning Electron Microscopy. In *Springer Handbook of Microscopy*; Hawkes, P.W., Spence, J.C.H., Eds.; Springer Nature: Berlin, Germany, 2019; pp. 229–318.
44. Irshad, H.M.; Farooq, A.; Hakeem, A.S.; Azeem, M.Z.; Ehsan, M.A. Electrochemical study of aluminum–cubic boron nitride composites synthesized via spark plasma sintering for engineering applications. *J. Alloys Compd.* **2023**, *965*, 171210. [CrossRef]
45. Klinger, M. More features, more tools, more CrysTBox. *J. Appl. Crystallogr.* **2017**, *50*, 1226–1234. [CrossRef]
46. Klinger, M.; Jäger, A. Crystallographic Tool Box (CrysTBox): Automated tools for transmission electron microscopists and crystallographers. *J. Appl. Crystallogr.* **2015**, *48*, 2012–2018. [CrossRef] [PubMed]
47. Klinger, M. *CrysTBox—Crystallographic Toolbox*; Institute of Physics of the Czech Academy of Sciences: Prague, Czech Republic, 2015.

48. Klinger, M.; Polívka, L.; Jäger, A.; Tyunina, M. Quantitative analysis of structural inhomogeneity in nanomaterials using transmission electron microscopy. *J. Appl. Crystallogr.* **2016**, *49*, 762–770. [CrossRef]
49. Waseda, Y.; Matsubara, E.; Shinoda, K. *X-ray Diffraction Crystallography*; Springer: New York, NY, USA, 2011.
50. Cullity, B.D.; Stock, S.R. *Elements of X-ray Diffraction*; Pearson Education Limited: Essex, UK, 2014.
51. Ehsan, M.A.; Kumar, A.M.; Suleiman, R.K.; Hakeem, A.S. Fabrication of thickness-controlled NiPd nanoalloy thin films as anticorrosive coatings on 316L SS substrates for application in marine environment. *Surf. Coat. Technol.* **2021**, *418*, 127253. [CrossRef]
52. Jeffries, Z.; Kline, A.H.; Zimmer, E.B. The determination of grain size in metals. *Trans. Metall. Soc. AIME* **1916**, *54*, 594–607.
53. Jeffries, Z. Grain-size measurements in metals, and importance of such information. *Trans. Faraday Soc.* **1917**, *12*, 40–53. [CrossRef]
54. Wyckoff, R.W. *Crystal Structures*, 2nd ed.; Interscience: New York, NY, USA, 1963; Volume 1.
55. Hjerten, I.; Werner, P.E.; Marinder, B.O.; Salwen, A. Structural investigations on the monoclinic sigma-phase in the Cr–Fe–Ni–Mo system. *Acta Chem. Scand.* **1982**, *36*, 203–206. [CrossRef]
56. Qian, W.; Zhang, W.; Wu, S.; Hu, Y.; Zhang, X.; Hu, Q.; Dong, S.; Tu, S. In situ X-ray imaging and numerical modeling of damage accumulation in C/SiC composites at temperatures up to 1200 °C. *Mater. Sci. Technol.* **2024**, *197*, 65–77. [CrossRef]
57. Bruemmer, S.M.; Simonen, E.P.; Scott, M.; Andresen, P.L.; Was, G.S.; Nelson, J.L. Radiation-induced material changes and susceptibility to intergranular failure of light-water-reactor core internals. *Nucl. Mater.* **1999**, *274*, 299–314. [CrossRef]
58. Bruemmer, S.M. *Grain Boundary Segregation in Austenitic Stainless Steels and Effects on Intergranular Stress Corrosion Cracking in Light-Water Reactor Environments*; CORROSION 98; NACE: San Diego, CA, USA, 1998.
59. Alshater, A.A.; Engelberg, D.L.; Donohoe, C.J.; Lyon, A.B.; Sherry, A.H. Proton irradiation damage in cold worked Nb-stabilized 20Cr-25Ni stainless steel. *Appl. Surf. Sci.* **2018**, *454*, 130–137. [CrossRef]
60. Andersen, A.G.; Jette, E.R. X-ray investigation of the Fe-Cr-Si phase diagram. *Trans. Am. Soc. Met.* **1936**, *24*, 375–419.
61. Badjuk, T.I.; Kushma, G.P.; Rybajlo, O.I. Temperature- and concentration dependence of the unit cell dimensions of Fe-Cr solid solutions. *Izv. Vyss. Uchebnykh Zaved. Chernaya Metall.* **1974**, *17*, 126–128.
62. Dorofeev, Y.A.; Men'shikov, A.Z.; Taksey, G.A. Magnetic phase diagram of Fex Cr1-x alloys. *Fiz. Met. Metalloved.* **1983**, *55*, 102–109.
63. Nishihara, Y.; Nakajima, Y.; Akashi, A.; Tsujino, N.; Takahashi, E.; Funakoshi, K.; Higo, Y. Isothermal compression of face-centered cubic iron. *Am. Mineral.* **2012**, *97*, 1417–1420. [CrossRef]
64. Oila, A.; Bull, S. Atomistic simulation of Fe-C austenite. *Comput. Mater. Sci.* **2009**, *45*, 235–239. [CrossRef]
65. Goldschmidt, H.J. Interplanar spacings of carbides in steels. *Metallurgia* **1949**, *40*, 103.
66. Yakel, H.L. Atom distributions in sigma phases. II. Estimations of average site-occupation parameters in a sigma phase containing Fe,Cr,Ni, Mo and Mn. *Acta Crystallogr. B* **1983**, *39*, 28–33. [CrossRef]
67. Bergman, G.; Shoemaker, D.P. The Determination of the Crystal Structure of the Phase in the Iron-Chromium and Iron-Molybdenum Systems. *Acta Crystallogr.* **1954**, *7*, 857–865. [CrossRef]
68. Guo, L.; Hua, G.; Yang, B.; Lu, H.; Qiao, L.; Yan, X.; Li, D. Electron work functions of ferrite and austenite phases in a duplex stainless steel and their adhesive forces with AFM silicon probe. *Sci. Rep.* **2016**, *6*, 20660. [CrossRef] [PubMed]